THE JOURNAL OF PHYSICAL CHEMISTRY C

Article

pubs.acs.org/JPCC

Charge Carrier Dynamics and Mobility Determined by Time-Resolved Terahertz Spectroscopy on Films of Nano-to-Micrometer-Sized Colloidal Tin(II) Monosulfide

Brian G. Alberding,[†] Adam J. Biacchi,[‡] Angela R. Hight Walker,[‡] and Edwin J. Heilweil*[,†]

[†]Radiation Physics Division and [‡]Engineering Physics Division, National Institute of Standards and Technology (NIST), 100 Bureau Drive, Gaithersburg, Maryland 20899, United States

Supporting Information

ABSTRACT: Tin(II) monosulfide (SnS) is a semiconductor material with an intermediate band gap, high absorption coefficient in the visible range, and earth abundant, nontoxic constituent elements. For these reasons, SnS has generated much interest for incorporation into optoelectronic devices, but little is known concerning the charge carrier dynamics, especially as measured by optical techniques. Here, as opposed to prior studies of vapor deposited films, phase-pure colloidal SnS was synthesized by solution chemistry in three size regimes, ranging from nanometer- to micrometer-scale (SnS small nanoparticles, SnS medium 2D nanosheets, and SnS large 2D μm-sheets), and evaluated by time-resolved terahertz spectroscopy (TRTS); an optical, noncontact probe of the photoconductivity. Dropcast films of the SnS colloids were studied by TRTS and compared to both thermally annealed films and dispersed suspensions of the same colloids. TRTS results revealed that the micrometer-scale SnS crystals and all of the annealed films undergo decay mechanisms during the first 200 ps following photoexcitation at 800 nm assigned to hot carrier cooling and carrier trapping. The charge carrier mobility of both the dropcast and annealed samples depends strongly on the size of the constituent colloids. The mobility of the SnS colloidal films, following the completion of the initial decays, ranged from 0.14 $cm^2/V{\cdot}s$ for the smallest SnS crystals to 20.3 $cm^2/V{\cdot}s$ for the largest. Annealing the colloidal films resulted in a ~20% improvement in mobility for the large SnS 2D μm-sheets and a ~5-fold increase for the small nanoparticles and medium nanosheets.

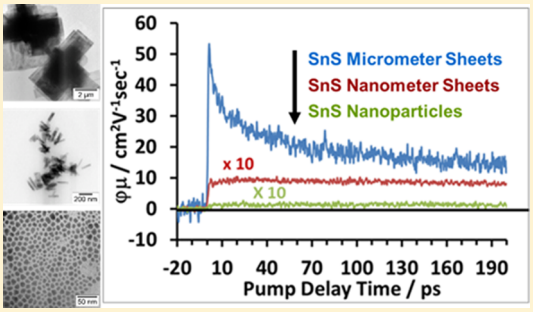

INTRODUCTION

Major roadblocks to the competiveness and implementation of photovoltaic devices are the cost and toxicity of constituent materials. Decreasing the cost can be accomplished by improving the efficiency of photon absorption to current generation by design of absorber, charge transport, and electrode layers, and/or by utilizing materials that are more earth abundant or easier to extract from natural sources.[1] Tin(II) monosulfide (SnS) is a material that is considered a potential candidate for next-generation optoelectronics, and has already been incorporated into photovoltaic devices.[2,3] It is an attractive material for these applications because tin and sulfur are both earth-abundant elements that are nontoxic. Additionally, SnS has optical properties comparable with silicon (Si). Both SnS and Si have indirect band gaps in the near-infrared (NIR) at 1.05 and 1.14 eV, respectively, with absorption coefficients that range from ~10^3 to 10^5 cm^{-1} from the NIR across the visible range.[4,5] These optical properties suggest that photovoltaics based on SnS as an alternative visible light absorber can theoretically reach 25% to 30%, although currently the performance has only reached 4% to 5%.[3]

Among the limitations that constrain the photovoltaic conversion efficiency are small carrier diffusion lengths within the SnS absorber material and poor band alignment between SnS and the other charge transport layers incorporated into the device. While much work has been done to alter device configuration and film layer morphology to optimize performance,[2] there are few reported studies to understand the fundamental dynamics of photogenerated charge carrier transport within SnS thin film materials, especially by optical techniques. In particular, time-resolved photoconductivity measurements are an optical probe of the photogenerated charge transfer and recombination kinetics, as well as the charge carrier mobility and conductivity, and do not require electrical contacts or fabrication of a complete device. Two such optical photoconductivity techniques are flash-photolysis time-resolved microwave conductivity (FP-TRMC)[6] and time-resolved terahertz spectroscopy (TRTS).[7,8] In FP-TRMC, dynamics can be followed on the nanosecond to microsecond time scale and information about electron−hole recombination are obtained. Conversely, with TRTS subpicosecond time resolution is available and information concerning charge separation, relaxation, and charge trapping processes can be measured out to the ~1 ns time scale. These experiments have

Received: February 18, 2016
Revised: June 23, 2016

DOI: 10.1021/acs.jpcc.6b01684
J. Phys. Chem. C XXXX, XXX, XXX−XXX

been done for a variety of bulk[9] and nanoparticle inorganic semiconductors,[10,11] dye-sensitized semiconductors,[12,13] composite nanostructures,[14−16] polymers,[17,18] perovskites,[19−21] and metal−organic frameworks.[22−24] Despite applicability to a wide variety of materials, only recently has the terahertz photoconductivity been reported in SnS thin films prepared by thermal evaporation and atomic layer deposition.[25]

One way to evaluate a potential material for electronic device applications is to determine the charge carrier mobility. Mobility values for SnS have been determined by van der Pauw Hall measurements (contact probe methods), and vary greatly from values around 10 $cm^2/V{\cdot}s$ to as high as ∼400 $cm^2/V{\cdot}s$ depending on the method of film growth, the grain size, and the intrinsic carrier type and concentration.[26] Epitaxially grown films show the highest mobility, assisted by fewer grain boundaries, while films consisting of smaller crystalline domains suffer from increased scattering at the boundaries.[27] Films of SnS with grain sizes of around 200 to 500 nm grown by thermal evaporation[28] or atomic layer deposition[5] were found to have mobilities between 20 and 40 $cm^2/V{\cdot}s$.

Herein, as opposed to recent studies of vapor deposited films,[25] the solution-phase synthesis of colloidal SnS crystals and characterization by TRTS is reported to gain insights into the effects of the size, morphology, and composition on the dynamics and mobility of photogenerated charge carriers. Crystalline SnS colloids with oleylamine surface ligands were synthesized using solution chemistry routes in three distinct size regimes ranging from the nanometer- to the micrometer-scale. The three size regimes are denoted throughout as SnS small (0D spherical nanoparticles, 10 ± 2 nm diameter), SnS medium (2D nanosheets, 149 ± 23 nm length by 41 ± 17 nm width and ∼25 nm thick), and SnS large (2D sheets, 4.8 ± 0.8 μm length by 1.2 ± 0.7 μm in width and ∼30 nm thick). TRTS experiments were performed on films and dispersed suspensions of these colloidal SnS crystals. These experiments revealed a strong dependence of the charge carrier dynamics and mobility on the size dimensions of the colloidal crystals. Additionally, when postdeposition annealing process was conducted, an improvement in the charge carrier mobility was observed and attributed to sintering of the colloidal crystallites and removal of the surface stabilizing ligands.

EXPERIMENTAL SECTION

Materials. Tin(IV) chloride (99.995%), tin(II) acetate, sulfur powder (99.98%), and oleylamine (70%, technical grade) were purchased from Sigma-Aldrich. Tin(II) chloride, hexamethyldisilazane (>99%), and thioacetamide (99%) were purchased from Alfa Aesar. Solvents, including toluene and ethanol, were of analytical grade. All chemicals were used as received.

Synthetic Details. All reactions were performed under an argon atmosphere using standard Schlenk techniques. Micrometer-scale SnS sheets (SnS large) were synthesized using a heat-up route. First, 0.0075 g (0.1 mmol) of thioacetamide (TA) was dissolved in 10 mL of oleylamine (OLAM) and then added to a 25 mL three-neck flask equipped with a condenser fitted to a Schlenk line. The reaction temperature was controlled using a digital controller with glass-coated thermocouple (Gemini, J-KEM Scientific) and a 25 mL heating mantle (Glas-Col). Next, 5.8 μL (0.05 mmol) of $SnCl_4$ was added while the solution was stirred vigorously with a magnetic stir bar. The flask was sealed with a septum before being evacuated. The reaction was heated to 120 °C and maintained at that temperature under vacuum for 20 min to remove residual water. After the reaction solution was placed under an argon blanket, 1 mL (4.8 mmol) of hexamethyldisilazane (HMDS) was injected through the septum with a syringe. The temperature was raised to 180 °C, causing the solution to turn from orange to dark brown, and maintained at that temperature for 1 h before quenching the reaction with cold water. SnS sheets were separated from the reaction solution by adding 30 mL of ethanol antisolvent and centrifuging at 5000 rpm for 1 min. After decanting the supernatant, the precipitate was redispersed in toluene and centrifuged at 13000 rpm for 1 min. The supernatant was discarded once again and the precipitate was redispersed in 2 mL of toluene.

Nanometer-scale SnS sheets (SnS medium) were synthesized using a similar route. 0.0118 g (0.05 mmol) of $Sn(OOCCH_3)_2$ and 0.0032 g (0.1 mmol) of sulfur were dissolved in 10 mL of OLAM then added to a 25 mL reaction flask that was equivalently outfitted. After heating at 120 °C for 20 min under vacuum, the reaction was put under an argon blanket and the temperature was raised to 180 °C. Upon reaching 180 °C, 0.75 mL (3.6 mmol) of HMDS was injected through the septum and the temperature was maintained for 1 h before quenching the reaction with cold water. The nanosheets were separated in the same manner as above.

SnS spherical nanoparticles (SnS small) were synthesized using a hot injection strategy. First, 0.0095 g (0.05 mmol) of $SnCl_2$ and 8.5 mL of OLAM were added to a similar 25 mL reaction setup. After maintaining the contents of the flask at 120 °C for 20 min under vacuum, all of the $SnCl_2$ had dissolved. One mL (4.8 mmol) of HMDS was injected into the flask under an argon blanket and the temperature was raised to 140 °C. Separately, 0.0075 g (0.1 mmol) of TA was dissolved in 1.5 mL of OLAM. The TA solution was injected into the reaction flask all at once through the septum, causing the solution to quickly turn from clear to dark brown. The reaction was maintained at 140 °C for 1 h and then quenched with cold water. SnS nanoparticles were collected in a similar manner, except centrifugation at 13000 rpm was conducted in 1:1 (by volume) toluene:ethanol instead of neat toluene.

Morphology and Composition Characterization. Transmission electron microscope (TEM) images were collected using a Phillips EM-400 transmission electron microscope operating at an accelerating voltage of 120 kV. Samples were prepared by casting one drop of dilute dispersed sample in toluene onto a 300-mesh Formvar and carbon-coated copper grid (Ted Pella, Inc.). Particle counting analysis used a minimum of 200 individual particles and size was determined using the ImageJ program.[50] Powder X-ray diffraction (XRD) patterns were collected with a Rigaku SmartLab X-ray Diffractometer in the Bragg−Brentano geometry using Cu Kα radiation. Samples were dropcast in toluene onto either a zero background plate or a fused quartz substrate. Simulated powder XRD patterns were made using the CrystalMaker software suite. Scanning electron microscope (SEM) images of dropcast films were obtained using a Zeiss NVision 40 field emission SEM operating at 3 kV. X-ray photoelectron spectroscopy (XPS) analyses were performed on a Kratos Axis Ultra X-ray photoelectron spectrometer with a monochromatic Al Kα excitation source operating at 15 kV and 10 mA. Samples were prepared by dropcasting the sample onto a gold-coated Si wafer.

Film Preparation and Characterization for Optical Measurements. Films of the small-, medium-, and large-sized

DOI: 10.1021/acs.jpcc.6b01684
J. Phys. Chem. C XXXX, XXX, XXX−XXX

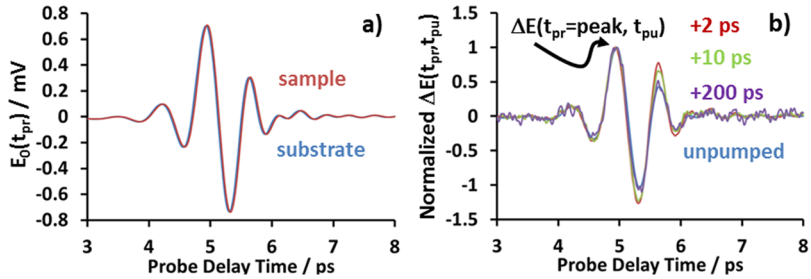

Figure 1. For the SnS large dropcast film: (a) representative measured transmission of the terahertz electric field, $E_0(t_{pr})$, through the sample (red) compared to the fused quartz substrate (blue); (b) representative differential transmission of the terahertz electric field, $\Delta E(t_{pr},t_{pu})$, through the excited film at pump delay time +2 ps (red), + 10 ps (green), + 200 ps (purple) normalized to the terahertz transmission, $E_0(t_{pr})$, through the unexcited film (unpumped). This shows there is no significant phase shift between the photoexcited and unphotoexcited samples. The true sign of the differential transmission is negative compared to the unexcited film, indicating that the transmission is *decreased* following photoexcitation.

SnS were prepared for TRTS measurements by dispensing a single drop of the toluene suspension onto a substrate disc of fused quartz (GM Associates, Inc., thickness 1/8 in., part no. 7500-02, or 1/16 in., part no. 7500-01) using a Pasteur pipet and allowing it to dry in air at room temperature. This generated dropcast films and resulted in sample spots that were approximately 5−6 mm in diameter. *Separate* samples were made for annealed films. Single drops of the small-, medium-, and large-sized SnS dropcast suspensions were again placed on fused quartz substrates, allowed to dry, and then annealed in a tube furnace (Lindburg/Blue M, Thermo Scientific) at 400 °C under 5% H_2 forming gas for 1 h. The dropcast and annealed films were stored in a closed container in air until the time that optical measurements were made. The average thickness of each sample spot was measured using a Bruker Dektak XT contact profilometer. The average thicknesses for the dropcast films are as follows: large, 2.50 μm; medium, 80 nm; small, 12.5 nm. The average thicknesses for the annealed films are as follows: large, 7.05 μm; medium, 1.56 μm; small, 267 nm. Annealing resulted in a noticeable reduction of the sample spot size, which could indicate that the film thickness is generally larger for the annealed films.

In order to investigate possible interactions between neighboring crystals in the films, dispersions of well-suspended, isolated colloids were also studied. Suspensions of the SnS large sheets and SnS medium nanosheets were prepared by dispersing them in mineral oil, a high viscosity solvent, and sonicating for 30 min, which allowed the particles to remain suspended during TRTS measurements. The SnS small nanoparticles formed more stable suspensions in toluene and were therefore used as prepared. The suspensions were transferred to a 1 mm thick quartz cuvette for TRTS and absorbance measurements.

Visible-NIR Transmission and Reflection Measurements. Transmission (T) measurements between 300 and 1100 nm were made on the SnS colloidal films using a PerkinElmer Lambda 2 UV−vis spectrometer. Reflection (R) spectra were also measured on the same films using a PerkinElmer Lambda 950 spectrometer equipped with an integrating sphere accessory set up for diffuse reflection acquisition. The diffuse reflectance setup was configured without a reference scattering material behind the sample in order to minimize any light transmitted through the sample from scattering back into the integrating sphere detector. This allowed the percent reflection of the sample to be measured independent from the percent transmission. In this way, the percentage of light absorbed (A) by the sample was estimated by the relation $A = 1 - R - T$. For all films, a blank spot on the substrate was used as a reference and the beam source was attenuated by an aperture set to the sample spot size. For the suspensions, all spectra were referenced to the solvent.

Time-Resolved Terahertz Spectroscopy. Charge carrier dynamics and mobility were determined by measuring the change in transmission of terahertz frequency probe pulses through the SnS samples following photoexcitation with 800 nm light. The apparatus is based on an amplified femtosecond Ti:sapphire laser system (Coherent MIRA seed and Legend regenerative amplifier) that operates at 1 kHz.[17] The amplified 800 nm pulse train (1.6 mJ/pulse and 40 fs full-width half-maximum pulse duration) is split into three arms for the visible pump, terahertz probe, and gated electro-optic detection. The first arm is directed down a delay stage and used for visible photoexcitation at 800 nm (beam diameter ∼5 mm, fwhm ∼50 fs, fluence ranging from 1×10^{12} to 5×10^{15} photons/cm^2). The second arm is directed down another delay stage and then onto a 1 mm thick zinc telluride (ZnTe) crystal to generate the terahertz frequency probe pulses by optical rectification. The generated probe pulses are then focused onto the sample (800 pJ/pulse measured by Gentec-eo T-RAD-USB detector, beam diameter ∼2 mm, 2 ps pulse width) by a pair of parabolic mirrors and transmitted through the sample. The third arm serves as the gate pulse for the electro-optic detection scheme. Here, the 800 nm pulses are attenuated and then recombined with the transmitted terahertz probe pulses in a 0.5 mm thick ZnTe detector crystal at various probe delay times, t_{pr}, to map out the terahertz pulse waveform. The electro-optic effect in the ZnTe detector crystal results in a depolarization of the 800 nm gate pulse that depends on the magnitude and sign of the electric field of the terahertz probe pulse. The resulting polarization in the 800 nm gate pulse is analyzed by a $\lambda/4$ wave plate and Wollaston prism, and then collected by a pair of balanced silicon photodetectors using lock-in amplification (Stanford Research Systems, SR830). Samples were mounted on an aperture set to the sample size and housed within a sample chamber purged with dry air to avoid absorption of the terahertz probe by atmospheric water. All measurements were done at room temperature.

The intrinsic conductivity of thin conductive materials can be determined from the transmission of the terahertz electric field, $E_0(t_{pr})$, through the sample compared to that transmitted through a blank reference substrate.[29,30] An example of the terahertz electric field transmitted through the SnS large dropcast film is shown in Figure 1a and compared to a blank spot on the fused quartz substrate as a reference. In the case of

DOI: 10.1021/acs.jpcc.6b01684
J. Phys. Chem. C XXXX, XXX, XXX−XXX

all the SnS films studied here (Figure S1), the electric field waveform for the film and reference are basically superimposable, which indicates that the intrinsic dopant level and conductivity of the films are quite low. Photoexcitation of the band gap transition in a semiconductor generates free charge carriers and leads to increased free carrier absorption and decreased terahertz transmission. The change in transmission of the terahertz probe, $\Delta E(t_{pr},t_{pu})$, at various pump−probe delay times, t_{pu}, is shown in Figure 1b normalized to the unphotoexcited sample transmission for the film of SnS large sheets. The change in electric field transmission can be related to the electrical photoconductivity of the sample by eq 1:

$$\sigma(\omega, t_{pu}) = -\left(\frac{n_{THz} + 1}{Z_0 d}\right)\frac{\Delta\tilde{E}(\omega, t_{pu})}{\tilde{E}_0(\omega)} \quad (1)$$

where $\Delta\tilde{E}(\omega,t_{pu})$ is the Fourier transform of the measured $\Delta E(t_{pr},t_{pu})$ of the photoexcited sample, $\tilde{E}_0(\omega)$ is the Fourier transform of the measured $E_0(t_{pr})$ of the nonphotoexcited sample, n_{THz} is the index of refraction of the substrate, Z_0 is the free space impedance, d is the film thickness (measured by profilometry), and $\sigma(\omega,t_{pu})$ is the transient complex-valued frequency-dependent photoconductivity change.[31,32] This equation was used to determine the frequency-dependent conductivity from measurements of ΔE and E_0. As shown in Figure 1b (and for all the other films, in Figure S2), there are some changes in the relative amplitude of the transmitted terahertz electric field in the wings of the waveform pulse that lead to changes in the frequency-dependent spectra described by eq 1, but there is no observed phase shift in the main peak of the pulse. The lack of phase shift indicates the samples can be considered as thin, photoconductive, films on insulating substrates and eq 1 can be represented as the frequency-averaged conductivity when the change in transmission is measured at the peak of the terahertz electric field, $\Delta E(t_{pr} = \text{peak}, t_{pu})$.[33] In that case, the measured conductivity can be considered as the direct current conductivity and the measured $\Delta E(t_{pr} = \text{peak}, t_{pu})$ can be related to the charge carrier mobility through $\sigma = eN\mu$ and eq 2:

$$\phi(t_{pu})\mu(t_{pu}) = -\left(\frac{n_{THz} + 1}{Z_0 eF(1 - R - T)}\right)\frac{\Delta E(t_{pr} = \text{peak}, t_{pu})}{E_0(t_{pr} = \text{peak})} \quad (2)$$

Here e is the electron charge, N is the photogenerated carrier density, $\phi(t_{pu})$ is the charge carrier generation efficiency, $\mu(t_{pu})$ is the charge carrier mobility, F is the fluence, and R and T are the percent reflection and percent transmission, respectively, of the visible pump beam from the sample.[33] The charge carrier density N was estimated by $N = \phi F(1 - R - T)/d$. Equation 2 was used to analyze the measured $\Delta E(t_{pr} = \text{peak}, t_{pu})$ and determine a lower bound to the charge carrier mobility for all samples as a function of pump−probe delay time, t_{pu}. The charge carrier mobility and recombination dynamics were also fit to double exponential decays of the form $\Delta E(t_{pu})/E_0 = A_1 \exp(-t_{pu}/\tau_1) + A_2 \exp(-t_{pu}/\tau_2) + y_0$, where A is the pre-exponential factor, τ is the lifetime, and y_0 is the long time delay time. The dynamics were also collected at various excitation fluences, and the signal magnitudes were found to be in the linear range with respect to pump power. The lifetimes were determined for each of the excitation fluences and averaged to obtain the values tabulated below in Table 1 where the error bars represent the standard deviation of the average (type B; $k = 1$ analysis).

RESULTS AND DISCUSSION

Morphology and Composition. Colloidal tin(II) monosulfide of three distinct size regimes was synthesized using solution chemistry routes developed specifically for this study. In general, these strategies were based on the thermal decomposition of tin and sulfur precursors in oleylamine solvent, which is a high boiling point surfactant (see Experimental Section for details).[34] The resulting ligand-stabilized, colloidal samples of SnS were dispersed in toluene prior to analysis. TEM imaging revealed that the sample of the largest crystals (SnS large, Figure 2a) formed micrometer-scale

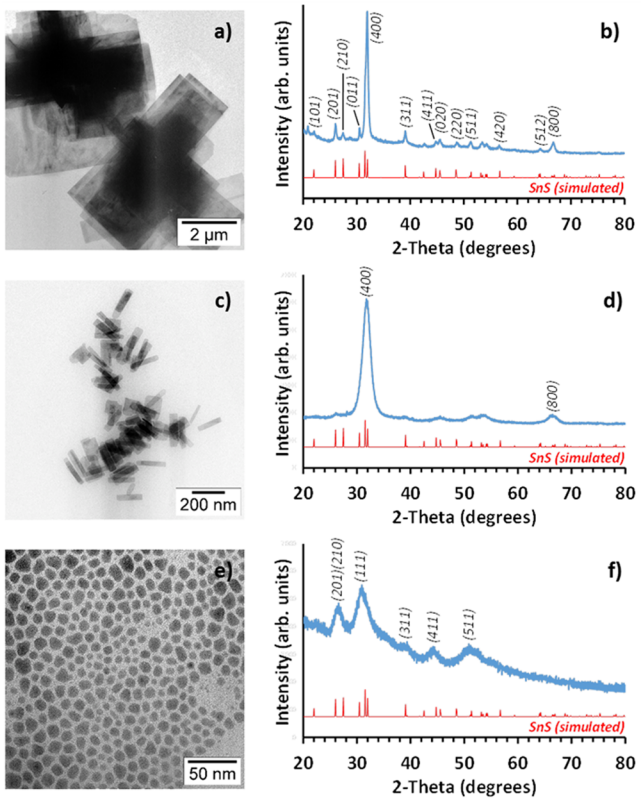

Figure 2. TEM images (left) and X-ray diffraction patterns (right) for the SnS large (a, b), SnS medium (c, d), and SnS small (e, f) films.

2D sheets of dimensions 4.8 ± 0.8 μm in length and 1.2 ± 0.7 μm wide. This morphology is expected, as bulk SnS crystallizes in the layered orthorhombic GeS-type structure, which favors the formation of belts and sheets.[35,36] The intermediate-sized sample also consisted of 2D structures, yielding nanosheets 149 ± 23 nm long and 41 ± 17 nm wide (SnS medium, Figure 2c). Finally, TEM analysis of the smallest-sized sample indicated that it comprised of nanoparticles 10 ± 2 nm in diameter of a roughly spherical morphology (SnS small, Figure 2e). Additional TEM images of these three samples are provided in Figure S3. Powder XRD patterns were also collected and compared to the simulated structure of GeS-type SnS (Figure 2b,d,f). All patterns reveal that the samples are phase-pure tin(II) monosulfide, although the SnS small pattern is consistent with a structural distortion that is known to occur in SnS 0D nanocrystals.[35] Further, the

DOI: 10.1021/acs.jpcc.6b01684
J. Phys. Chem. C XXXX, XXX, XXX−XXX

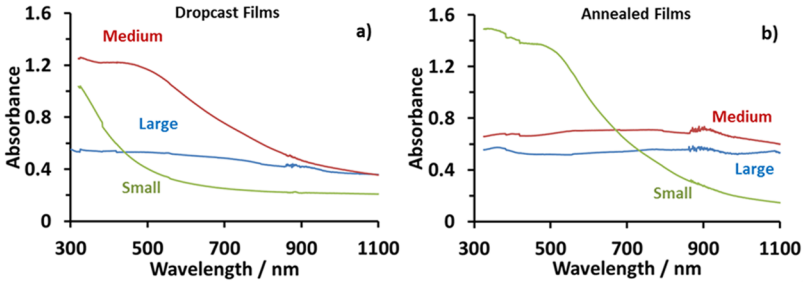

Figure 3. Absorption spectra derived from $-\log(R + T)$ scaled to a blank substrate of the (a) dropcast and (b) annealed SnS films on fused quartz substrates at room temperature. Note: There is a detector change at 870 nm.

patterns of the large and medium samples indicate substantial preferred orientation of the (400)/(800) planes, as expected for 2D sheets, with substantially sharper reflections observed in the large pattern, confirming their larger crystalline domain size. Importantly, the most intense reflection of the smallest sample is broad and centered on SnS(111), denoting a smaller domain size and lack of preferred orientation, indicative of spherical nanoparticles.

Films of SnS for optical analysis were prepared from solution by dropcasting onto fused quartz substrates. In order to examine the effect of heat treatment, separate films of each size regime were fabricated and annealed in a tube furnace at 400 °C under 5% H_2 forming gas for comparison to the nonannealed dropcast samples. Powder XRD patterns of the as-deposited and annealed SnS films are displayed in Figure S4. Despite the high background noise generated by the quartz substrate, the reflections for the small and medium size regimes are clearly observed to sharpen following heating, indicating an increase in crystalline domain size. This suggests that sintering is occurring during the annealing process. The effect is most pronounced for the small nanoparticles, owing to their high surface area which promotes interaction between neighboring nanoparticles. Conversely, the film composed of large micrometer crystals displayed only a modest increase in average domain size (Figure S4).

SEM imaging of the films (Figure S5) further corroborates the XRD results. Comparison of the images before and after treatment indicate that a substantial amount of organic material, which is clearly seen coating the SnS prior to annealing (Figures S5a,c,e) is removed, allowing for more intimate contact between individual crystals. The morphology and size of the micrometer-scale sheets was largely retained, and several crystals lying perpendicular to the substrate were on the order of 30 nm thick, confirming their 2D nature. Crystals of the medium SnS nanoscale sheets became more rounded, nonuniform, and networked after furnace treatment (Figure S5d), indicating that sintering had taken place, as suggested by our XRD analysis. However, the effect of sintering was even more dramatic in the film composed of small SnS. SEM revealed that plate-like crystals, of a similar morphology to the medium SnS film, roughly 100 nm long and 25 nm thick had formed from the spherical 10 nm diameter nanoparticles. Once again, this is in agreement with the XRD results seen in Figure S4. Additionally, while the dropcast film of SnS small nanoparticles dried in such a manner that voids developed (Figure S5e), annealing resulted in a more cohesive film (Figure S5f).

The chemical states of the surface atoms before and after heating were investigated using XPS (Figure S6). High-resolution scans of the Sn 3d region revealed that a mixture of Sn oxidation states was present prior to heat treatment, with a substantial Sn^{4+} contribution, likely due to tin oxide (SnO_2), on the surface. Following annealing, the signal can primarily be attributed to Sn^{2+}, indicating that the vast majority of the oxide layer was removed from the surface, exposing the underlying bulk SnS. Additionally, the Sn 3d spectrum displayed an improved degree of chemical state uniformity, which suggests that heating may also have improved the quality of the SnS crystal by removing any defects and vacancies present at the surface. High-resolution XPS studies of the N 1s region confirmed that substantial nitrogen was present on the as-deposited dropcast films due to oleylamine ligand stabilizers still adsorbed to the surface of the SnS crystals. Heating the films at 400 °C removes these molecules, as observed by the lack of a substantial nitrogen peak in the XPS spectrum of the annealed film. This treatment engenders a clean surface that can more easily form intimate contact at the interface of adjoining crystals, promoting both sintering and improved charge carrier transfer.

Visible Absorption Spectroscopy. Absorption spectra of the three dropcast SnS films derived from transmission (T) and diffuse reflection (R) measurements are shown in Figure 3a. Bulk SnS has an indirect band gap of 1.05 eV,[4,37] while quantum confined nanoscale SnS can have a band gap several tenths of an electronvolt larger.[38] For the SnS small nanoparticles, the observed absorption feature tails into the visible range, giving rise to a brown-orange color, and peaks at wavelengths <300 nm. The absorption occurs at lower energy for the medium-sized 2D nanosheets and appears to have multiple features; one peaking in the ultraviolet at ∼300 nm and the other peaking at ∼500 nm and tailing into the near-infrared (NIR). For the large-sized 2D μm-sheets, the observed spectrum is featureless across the detected range and there is no direct indication of the absorption edge, consistent with the band gap known for bulk SnS occurring at 1180 nm. Because the SnS large film consists of μm-sized colloids, we attribute the observed spectral characteristics to scattering effects. Although the SnS large film has a larger thickness (measured by profilometry) compared to SnS small and SnS medium, the overall absorbance tends to be reduced due to increased scatter, which we have taken into account by measuring both transmission and reflection and calculating $-\log(R + T)$.

Shown in Figure 3b are the absorption spectra for annealed SnS films. In each case, annealing leads to a change in the observed absorption that suggests the crystals have sintered and grown in size.[28] For the small particles, the absorption has red-shifted and now tails into the NIR while the medium- and large-sized films now both appear flat and featureless throughout the detected range. We again attribute the featureless spectrum as an indication of increased scatter, which arises in the SnS medium film due to their increase in

DOI: 10.1021/acs.jpcc.6b01684
J. Phys. Chem. C XXXX, XXX, XXX−XXX

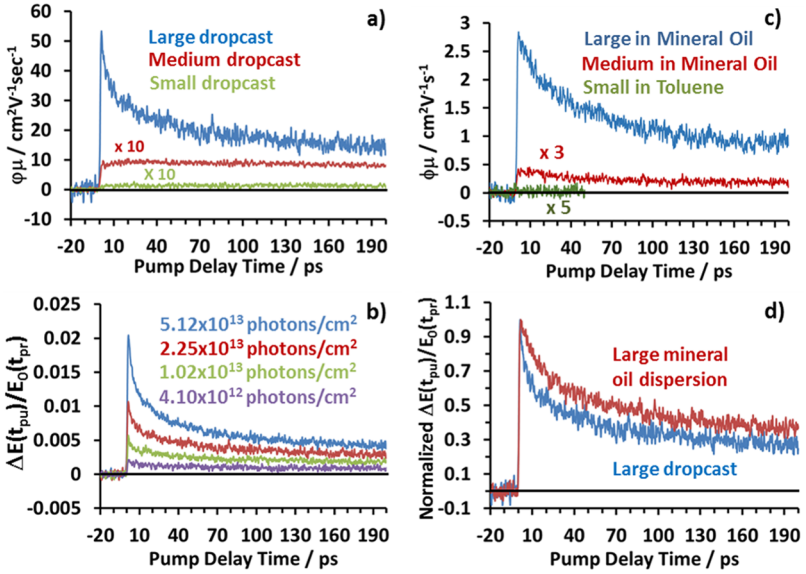

Figure 4. (a) Time dependence of the product of the charge carrier photogeneration yield and mobility derived from the measurements of $\Delta E(t_{pr}$ = peak, $t_{pu})/E_0(t_{pr}$ = peak) for the large (2.25×10^{13} photons/cm^2), medium (6.15×10^{14} photons/cm^2), and small (1.02×10^{15} photons/cm^2) SnS films at 298 K following photoexcitation at 800 nm. (b) Fluence dependence of $\Delta E(t_{pr}$ = peak, $t_{pu})/E_0(t_{pr}$ = peak) for the SnS large sheets dropcast sample. (c) Time-dependence of the product of the charge carrier photogeneration yield and mobility for suspensions of SnS large (1.02×10^{14} photons/cm^2), medium (5.12×10^{14} photons/cm^2), and small (8.20×10^{14} photons/cm^2) colloids following photoexcitation at 400 nm. d) Normalized comparison of $\Delta E(t_{pr}$ = peak, $t_{pu})/E_0(t_{pr}$ = peak) for the SnS large sheets as a dropcast film and dispersed in mineral oil following photoexcitation at 800 nm.

crystalline domain size. Importantly, these spectra also aid in the calculation of mobility values using eq 2 by roughly approximating the percent absorbance $(1 - R - T)$ of photons at the excitation wavelength.

Time-Resolved Terahertz Spectroscopy. *a. Pump-Delay Scans of Dropcast Films.* In order to measure the time-dependent photoconductivity, TRTS experiments were carried out on the SnS films following photoexcitation at 800 nm. Figure 4a shows results from the TRTS experiments for the small-, medium-, and large-sized SnS colloidal films, where the measurements of $\Delta E(t_{pr}$ = peak, $t_{pu})$ have been converted by eq 2 to units characteristic of the product of charge carrier mobility, $\mu(t_{pu})$, and photogeneration yield, $\phi(t_{pu})$. This analysis assumes the photogeneration yield is 100% and therefore the reported values represent a lower bound to the charge carrier mobility. The spectra shown in Figure 4a have also been scaled to account for any differences in percent absorption (Figure 3) of the excitation photons and any differences in the photodopant level (i.e., the excitation fluence, F) between the films. Note that the fluence dependence of the measured signal, $\Delta E(t_{pr}$ = peak, $t_{pu})$, was found to be within the linear range for all films. The calculated mobility, however, is not constant with respect to the excitation fluence due to additional carrier scattering at higher photodopant levels. Plots of the fluence dependence of the calculated mobility (Figure S7) for each of the films and the measured signal for representative films (Figure S8) can be found in the Supporting Information.

Figure 4a shows the photoconductivity responses of the films differ in two ways. First, for the film of SnS large sheets, the charge carrier dynamics are represented by a double exponential decay with lifetimes of $\tau_1 = 3.4 \pm 1.2$ ps and $\tau_2 = 52.4 \pm 7.5$ ps that relaxes to an offset that is longer lived than the 200 ps time scale of the experiment. Conversely, the films of the SnS medium nanosheets and SnS small nanoparticles do not exhibit any significant dynamic processes that occur within the first 200 ps. Second, the charge carrier mobility depends upon the colloid size dimensions and is biggest for the film of SnS large sheets. The SnS large film has a peak mobility of ~55 cm^2/V·s and attains a mobility of ~15 cm^2/V·s at 200 ps time delay whereas the medium- and small-sized films have mobility values of 0.8 and 0.1 cm^2/V·s, respectively, during the first 200 ps following photoexcitation at the fluence indicated for Figure 4a.

These mobility values permit estimation of the carrier diffusion length, $D = (\tau \mu K_b T/e)^{1/2}$, where τ is the free carrier lifetime and K_b is the Boltzmann constant. Because of the observed long-time offset, the lifetime of the longest decay process is not known, but we can equivalently consider the diffusion length for a given delay time at room temperature. For the SnS large sheets, the peak mobility indicates a diffusion length of 27 nm on the ~5 ps time scale, and the offset mobility indicates a diffusion length of 88 nm on the 200 ps time scale. These distances are much smaller than the size dimensions of the 2D plane but indicate charge carriers excited out-of-plane (due to random orientations of the 2D colloids in the film, indicated by SEM and TEM) could potentially interact with the surfaces along the thickness (~25−30 nm) dimension.

Similarly, the diffusion lengths for the SnS medium nanosheets and SnS nanoparticles were 20 and 7 nm, respectively, on the 200 ps time scale. These diffusion lengths suggest photogenerated charge carriers are strongly influenced by interactions with the colloid boundaries within their lifetime and within the 200 ps limit of the experiment for the 2D nanosheets and nanoparticles. In the 2D nanosheets, charge carriers could potentially interact with surfaces within the ~40 nm width of the 2D plane or out-of-plane along the ~25 nm thickness dimension. While the 2D sheets are single-crystalline, the nanoparticles have a lack of preferred orientation (by XRD) and likely consist multiple smaller crystalline

DOI: 10.1021/acs.jpcc.6b01684
J. Phys. Chem. C XXXX, XXX, XXX−XXX

domains due to their spherical shape. The small mobility and diffusion length for the 10 nm diameter nanoparticles therefore indicates charge carriers are strongly limited by interactions from these domain boundaries. The dependence of the observed mobility with particle size is therefore attributed to confinement of the charge carriers to the nanoscale dimensions within the colloids, which has been observed for other nanoscale semiconductor materials.[10,12]

Sources of the two decay components in the SnS large film can also be considered. According to eq 2, there are two effects that lead to a loss in the time-dependent photoconductivity: a decrease in the mobility or a loss in the number of free charge carriers.[39] A loss of free charge carriers can result from electron−hole recombination or charge trapping into impurity states. A decrease in charge mobility could occur due to cooling of initially hot, photoexcited charge carriers or a conversion to a conduction band state of different inherent mobility. An example of the latter is the behavior of GaAs, where high energy excitation leads to an internal conversion process to the Γ valley, which has higher inherent mobility.[40] Alternatively, intraband relaxation to the band edge, where the density of states can be smaller due to defects in the long-range crystalline order, can also result in lower mobility.[11,41]

Hot carrier cooling (or relaxation within the initially excited band structure) is one possible assignment for the fastest decay component of ∼3.4 ± 1.2 ps in the SnS large film. First, the generation of hot carriers is dependent upon the amount of excess energy provided by the excitation pulse compared to the absorption band edge for the band gap transition.[42] The SnS large sheets possess significant excess energy at 800 nm excitation compared to the band gap energy (1.55 vs 1.05 ev), and this could explain the absence of a picosecond time scale decay component in the SnS small and medium films. Excitation at 400 nm did not produce major changes in the observed dynamics (Figure S9). This is expected for the film of large SnS sheets, as the excitation wavelengths used are both above the band gap. Fits of the decay dynamics at 400 nm excitation did result in a slight increase to the observed lifetimes with τ_1 = 5.8 ± 0.2 ps and τ_2 = 63 ± 2 ps, so this could indicate a slightly longer thermalization time. For the nanosheets and nanoparticles, any ultrafast decay processes at our excitation wavelegnths could be beyond our time resolution. Second, relaxation of hot carriers to the band edge typically occurs on ∼100 fs time scale but it has also been found to occur on the 1 ps time scale in semiconductor nanomaterials.[42,43] Longer cooling lifetimes have also been reported for larger-sized particles[44] and in extended films.[45]

A second concomitant decay process occurs on the ∼52.4 ± 7.5 ps time scale. This can be associated with recombination or charge trapping processes, which leads to a decrease in photoconductivity due to a loss in the number of free charge carriers. It is not likely that this second decay process is associated with electron−hole recombination because the decay dynamics observed here are defined by an offset that lasts longer than the 200 ps of this experiment. Another possibility for this decay component, as well as the shorter ∼3 ps component, is Auger recombination, which can occur with lifetimes on the order of 10s of picoseconds and with lifetimes that are inversely proportional to excitation power.[46,47] Fluence dependence of the photoconductivity measured for the SnS large film aids the investigation of this possibility and is shown in Figure 4b. Fits of the decay dynamics at each excitation fluence show that neither lifetime is strongly dependent upon excitation power (Figure S10). Therefore, our results do not provide direct evidence to support Auger recombination processes in these films.

From the XPS studies, the dropcast films have a significant population of Sn^{4+} within the first 5−10 nm of the depth, and so charge trapping at the surface is also a possibility. This hypothesis can also be tested by the fluence dependence, where the rate of charge trapping at the surface should decrease for higher excitation fluence as the trap states become saturated with free charge carriers.[48,49] The observed dependence of the second decay lifetime on excitation power is also not consistent with this explanation. While the small- and medium-sized films could undergo very fast charge trapping at the surface due to their smaller domain size, it is apparent that the SnS large sheets are not strongly affected by SnO_2 states at the surface within the first 200 ps following excitation.

On the basis of the lack of fluence dependence, it is proposed that the second decay process is associated with charge trapping/localization into defect states near the band edge (such as Sn^{2+} or S^{2-} vacancies, excess Sn or S atoms, or other impurities leading to a smaller density of states) within the crystals for SnS large film. Very recently, the TRTS response of SnS thin films fabricated by thermal evaporation and atomic layer deposition was reported.[25] In that case only a single ∼70 ps decay process was reported and assigned as the minority carrier lifetime due to defect assisted recombination. Those results are consistent with the dynamics presented here and that assignment offers another plausible interpretation of the ∼50 ps decay.

b. Pump-Delay Scans of Dispersed Suspensions. In order to gain a better understanding of how the TRTS response for the dropcast films may depend on interactions between neighboring crystals in the film, TRTS experiments were also completed for each SnS colloidal size regime in suspension. In this way, the individual colloids are well-separated and the TRTS response can be attributed to an average over the distribution of colloid sizes and their random orientation in suspension. The results for these suspensions are shown in Figure 4c. The medium SnS nanosheets and large SnS sheets were dispersed in high viscosity mineral oil to maintain the suspension during the experiments but the small SnS nanoparticles form stable suspensions in toluene. 400 nm excitation was chosen to ensure adequate excitation optical density (Figure S11). These experiments show nearly the same trends observed for the dropcast films (Figure 4a) and reinforce our contention that the photogenerated charge carrier mobility is strongly dependent on the size dimensions and orientation of the constituent colloids. The SnS large sheets, which have micrometer-sized dimensions in the 2D plane show by far the largest charge carrier mobility compared to the medium nanosheets and small nanoparticles.

The mobility values determined for each sample in well-dispersed suspension is reduced significantly compared to the corresponding dropcast films. We could not observe any TRTS response for even the highest power pump pulse conditions for the suspension of SnS small nanoparticles. This suggests that the charge carriers confined to the 10 nm diameter nanoparticles do not provide sufficiently large conductivity to be measured in the dispersed suspension but the film of SnS nanoparticles has a larger charge carrier mobility due to interparticle interactions that allow some hopping between adjacent colloids, as suggested earlier for films composed of

DOI: 10.1021/acs.jpcc.6b01684
J. Phys. Chem. C XXXX, XXX, XXX−XXX

sub-10 nm semiconductor nanoparticles with surface stabilizing ligands.[11]

While some contribution from interparticle hopping could be present in the films of 2D sheets, the TEM and SEM images show that these colloids mostly lie parallel to the substrate plane and the greatest contribution to the mobility likely comes from charge carriers transported within the 2D micrometer dimensions. This would not be the case in the suspension where random orientations lead to a greater contribution of charge carriers moving along the much thinner thickness dimension (or reduced terahertz absorption cross section along this dimension) and therefore a much smaller average mobility. This argument can be similarly made for the medium nanosheets. However, the smaller nanoscale dimensions of the 2D plane likely leads to the lower mobility compared to the large sheets. We suggest the reduction in mobility observed in the suspended large colloids compared to the corresponding film most strongly originates from orientation effects rather than elimination of interparticle hopping in the films, whereas in the medium colloids, it could be a combination of both effects.

A comparison of the dynamics observed following 800 nm excitation in the film and suspension of the SnS large sheets is shown in Figure 4d. Here, it can be seen that the dynamics are nearly the same and contain two decay processes. The extracted initial decay lifetime increased from 3.4 ± 1.2 to 12.7 ± 2.2 ps while the second decay lifetime was 78.8 ± 16.2 ps, similar to that for the dropcast film. This presents further evidence that the charge carrier dynamics observed on the 200 ps time scale is largely confined to individual colloids in the SnS large sheets either as a film or as a suspension, however orientation effects are more important in suspension and results in lower average carrier mobility.

c. Frequency-Dependent Spectra of the Dropcast films. The frequency dependence of the photoconductivity for the SnS dropcast films was also determined. In this case, the terahertz waveform, $\Delta E(t_{pr},t_{pu})$, transmitted through the photoexcited sample was measured at fixed pump delay times, t_{pu}, and compared to the terahertz waveform without photoexcitation, $E_0(t_{pr})$, at the indicated excitation fluences. Fourier transforms of these terahertz waveforms were analyzed using eq 1, where the film thicknesses were obtained by profilometry. This analysis yielded the spectra shown in Figure 5, where the complex-valued photoconductivity has been separated into its real, $\Delta\sigma_1$, and imaginary, $\Delta\sigma_2$, parts.

It can be seen that there is a significant difference in the magnitudes of the real photoconductivity between the SnS small, medium, and large films. Upon initial inspection, it would appear the conductivity calculated by eq 1 for the SnS small nanoparticles was larger than that of the medium- and large-sized sheets based on the average magnitude of $\Delta\sigma_1$. The film of SnS small nanoparticles had a photoconductivity on the order of 30 ohm^{-1} cm^{-1}, whereas the film of SnS large sheets had a photoconductivity on the order of 1.0 $ohm^{-1}cm^{-1}$ at a 200 ps pump time delay. This arose because a much higher fluence was required to obtain a measurable signal in the films of smaller crystallite size. If the data for $\Delta\sigma_1$ shown in Figure 5 are averaged over the detected frequency range, the mobility can be calculated using the relation $\sigma = eN\mu$ and estimating the carrier density as $N = \phi F(1 - R - T)/d$, as described in the Experimental Section. This analysis yielded mobility values of 0.18, 0.75, and 10.5 $cm^2/V{\cdot}s$ for films of the SnS small-, medium-, and large-sized colloids, respectively which are

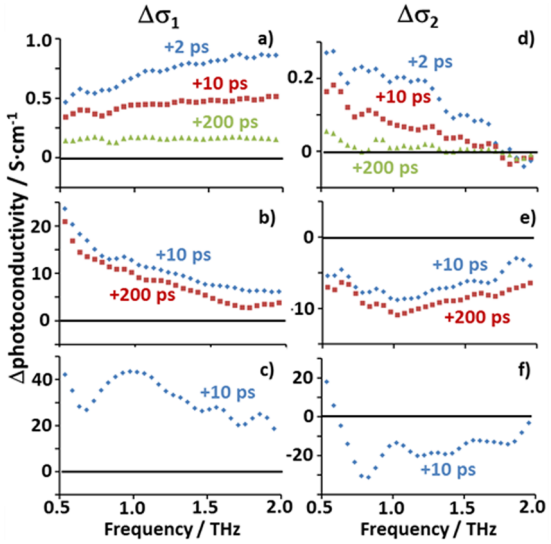

Figure 5. Frequency-dependent complex photoconductivity changes for the SnS dropcast films at the indicated pump−probe time delays. The real parts, $\Delta\sigma_1$, are shown on the left and the imaginary parts, $\Delta\sigma_2$, on the right for the large (a, d) medium (b, e) and small (c, f) samples. The fluence used for each experiment was 5.1 × 10^{13} photons/cm^2 (SnS large), 1.2 × 10^{15} photons/cm^2 (SnS medium), and 4.1 × 10^{15} photons/cm^2 (SnS small).

consistent with the trends determined from the analysis using eq 2 of the pump scan dynamics in part a, Figure 4a.

Another important difference between the three samples in the frequency-resolved photoconductivity spectra is the sign of the transient photoconductivity change following photoexcitation. For SnS large, both the real and imaginary parts are positive, but the real part is slightly increasing with frequency while the imaginary part is decreasing with frequency. This is true at each time delay across the observed 200 ps time range, where the conductivity magnitude follows the decay in the pump scan dynamics. Conversely, both the SnS small and SnS medium films have similar frequency-dependent spectra, with a positive real component and negative imaginary component of the photoconductivity. For these films, the real parts decrease with increasing frequency, while the imaginary parts slope back toward zero.

The sign of the transient photoconductivity reveals a size-dependence of the charge carrier dynamics observed in the SnS colloidal films. That the imaginary component is negative for the small- and medium-sized films suggests that the frequency-dependent conductivity is representative of the Drude−Smith model.[9] From this model, a negative imaginary component arises from scattering of the free charge carriers from the crystallite surfaces or grain boundaries. This results in the localization of charges within individual crystalline domains and reduces the mean free path.[12] In contrast, the positive imaginary component of the SnS large sheets suggests that the frequency-dependent conductivity can be characterized by a Drude-like response.[9] This indicates that scattering from the crystal surfaces or grain boundaries is not the dominating effect on the charge carrier mobility. Although the photogenerated free charge carriers are confined to individual crystals within the film of SnS large sheets, they do not experience significant scattering from grain or surface boundaries during the first 200 ps following excitation. Scattering from grain or surface boundaries, however, is quite significant for films of both the

DOI: 10.1021/acs.jpcc.6b01684
J. Phys. Chem. C XXXX, XXX, XXX−XXX

small- and medium-sized colloids due to their nanometer-scale crystalline domain size and this is likely the limiting factor on the charge carrier mobility.

d. Pump Delay Scans of the Annealed Films. In order to better understand the role played by the surface ligands on the charge carrier dynamics, dropcast SnS films were annealed at 400 °C in a tube furnace under 5% H_2 forming gas. The annealing process removes the oleylamine molecular stabilizer, resulting in a more pristine and uniform surface chemical environment (Figure S5 and S6). The annealed dropcast films of the small-, medium-, and large-sized colloids were also studied by TRTS using 800 nm excitation, and Figure 6 shows

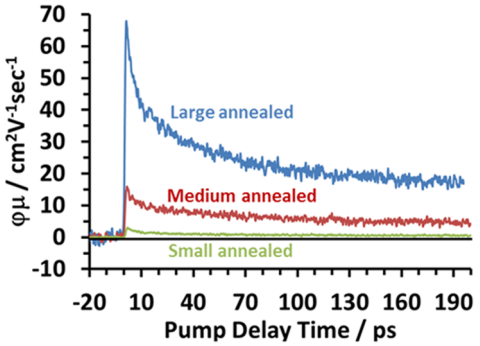

Figure 6. Time dependence of the product of the charge carrier photogeneration yield and the mobility derived from the measurements of $\Delta E(t_{pr}$ = peak, $t_{pu})/E_0(t_{pr}$ = peak) for post annealed films of the large (2.3×10^{13} photons/cm^2), medium (5.1×10^{13} photons/cm^2), and small (2.5×10^{14} photons/cm^2) SnS films at a specific excitation fluence.

the time dependence of the charge carrier mobility out to a 200 ps probe delay. For the SnS large annealed film, the transient photoconductivity response is very similar to that of the unannealed dropcast film. The dynamics again contain two decay components with each lifetime similar to those for the dropcast film (Figure S12), although there is a slight, ∼20% improvement in the charge carrier mobility during the 200 ps time frame following photoexcitation. Because there was no significant change to the observed decay dynamics, it could indicate that defect-assisted trapping mechanism is not responsible for the observed decay, as suggested above. Typically, annealing leads to a decrease in defect or impurity states which results in longer minority carrier lifetimes. This was observed by Jaramillo et al.[25] but is not the case for the SnS films studied here

More substantial changes occurred as a result of annealing the small- and medium-sized SnS films. For both, the mobility improved significantly, and now two components from the decay dynamics can be analyzed. As summarized in Table 1, the small- and medium-sized colloid films developed ∼3−4 ps and ∼50−60 ps decays that are, within error, equivalent to those observed for the SnS large films (both dropcast and annealed). The ∼3−4 ps component is interpreted equivalently to the dropcast films. Similarly, the ∼50−60 ps process is associated with charge carrier localization/trapping, and its observation in the annealed films substantiates our hypothesis that trapping at surface defect SnO_2 states does not occur. XPS results further substantiate this because the surface SnO_2 states appear to be largely removed from the annealed samples (Figure S6). It is apparent from the change in dynamics that the small- and medium-sized colloid films have developed characteristics similar to the SnS large film after annealing. This is due to heating and removal of the ligands, which caused the SnS crystals to sinter, increase in domain size and form more intimate contact between neighboring crystals, as confirmed by XRD (Figure S4) and SEM (Figure S5). However, the mobilities remain lower, because the domain size of the annealed SnS small nanoparticle film and medium 2D nanosheet film are still smaller compared to the SnS large μm 2D sheets.

e. Frequency-Dependent Spectra of Annealed Films. Additional information on the effect of annealing the films can be garnered from the frequency-dependent photoconductivity spectra shown in Figure 7. First of all, the magnitudes of $\Delta\sigma_1$ can again be averaged and the mobility calculated from $\sigma = eN\mu$ and $N = \phi F(1 - R - T)/d$. Using the data at 200 ps time delay, this was determined to be 0.27, 1.49, and 14.0 cm^2/V·s. Again, these trends are in agreement with the mobility values determined from the peak $\Delta E/E_0$ measurements and show the mobility of each film has increased as a result of annealing. These frequency-dependent measurements have only been collected at a single excitation fluence. In order to best interpret the mobility improvement that occurs with annealing, it is more appropriate to compare the films across a range of excitation fluences. This is shown in Figure S7 and indicates that in general the annealed films can achieve measurable $\Delta E/E_0$ levels while requiring smaller incident pump fluence, which is an indication of their higher charge mobility.

Table 1. Summary of the Parameters Derived from the Pump Delay Scans of $\Delta E(t_{pr}$ = peak, $t_{pu})/E_0(t_{pr}$ = peak) Following 800 nm Excitation

sample	τ_1 (ps)[a]	τ_2 (ps)[a]	μ(peak)[b] (cm^2 V^{-1} s^{-1})	μ(offset)[b] (cm^2 V^{-1} s^{-1})	$\Delta E/E$(peak)[b]	$\Delta E/E$(offset)[b]	fluence (photons/cm^2)
SnS small	NA[c]	NA	NA	0.14	NA	8.9×10^{-3}	1.0×10^{15}
SnS medium	NA	NA	NA	0.93	NA	6.7×10^{-3}	6.1×10^{14}
SnS large	3.4 ± 1.2	52.4 ± 7.5	59.5	20.3	5.4×10^{-3}	1.8×10^{-3}	1.0×10^{13}
SnS large in mineral oil	12.7 ± 2.2	78.8 ± 16.2	18.4	6.9	7.9×10^{-3}	2.9×10^{-3}	2.3×10^{13}
SnS large annealed	4.8 ± 1.2	62.8 ± 15.0	74.2	23.4	8.5×10^{-3}	2.7×10^{-3}	1.0×10^{13}
SnS medium annealed	3.7 ± 1.7	59.1 ± 7.7	15.2	5.0	1.2×10^{-2}	3.9×10^{-3}	5.1×10^{13}
SnS small annealed	3.4± 1.1	52.0 ± 5.1	2.9	0.52	9.1×10^{-3}	1.6×10^{-3}	2.5×10^{14}

[a]The lifetimes reported are an average value of those obtained at each fluence. The error bars are the standard deviation of the average. For each film there is also a longer-lived offset component. [b]These values are reported for the indicated fluence. Peak refers to the maximum of the pump delay scan while offset refers to the value at t_{pu} = 200 ps. Note that the mobility is fluence dependent and higher mobility values are generally determined at smaller fluence. [c]NA = Not applicable.

DOI: 10.1021/acs.jpcc.6b01684
J. Phys. Chem. C XXXX, XXX, XXX−XXX

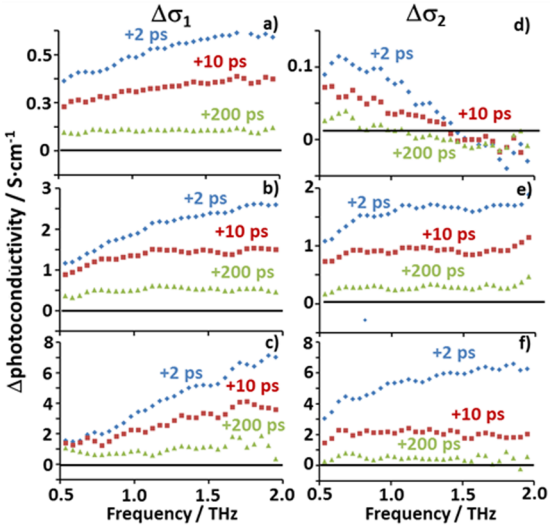

Figure 7. Frequency-dependent complex photoconductivity change of the SnS annealed films at the indicated pump−probe time delays. The real parts, $\Delta\sigma_1$, are shown on the left and the imaginary parts, $\Delta\sigma_2$ on the right for the large (a, d), medium (b, e), and small (c, f) SnS films. The fluence used for each of the samples was 1.0×10^{15} photons/cm^2 (SnS small annealed), 4.1×10^{14} photons/cm^2 (SnS medium annealed), and 5.1×10^{13} photons/cm^2 (SnS large annealed).

The main focus of the frequency-dependent measurements is to show how the spectral characteristics change with annealing. Now, both $\Delta\sigma_1$ and $\Delta\sigma_2$ are positive in all three of the annealed SnS films, which indicates the photoconductivity is characteristic of a Drude-like response.[9] It is thus apparent that the photogenerated charge carriers in the annealed SnS small nanoparticles and SnS medium 2D nanosheets are no longer significantly affected by back scattering from crystalline domain or surface boundaries. Two possibilities may lead to this result. One is that the constituent SnS crystals have sintered together due to the annealing process such that the charge carriers no longer reach the boundaries of the larger crystalline domains within 200 ps. If this were the case, however, it is expected that the mobility values would rise to a level comparable with that of the SnS large films. Because the mobility remains low, it suggests that the final colloid dimensions are still smaller than the micrometer-scale SnS large sheets, even though the crystalline domain size for the SnS small and SnS medium annealed films has increased (supported by SEM). A second proposed explanation for the absence of backscattering is that the charge carriers can be transferred through the film between individual crystalline domains. Increased interaction between neighboring crystals can be facilitated by removal of the surface molecular stabilizer and a decrease in the thickness of the surface oxide layer, which is supported by XPS. Improved charge transport across the domain boundaries in these annealed films would result in limited backscattering, but still lower mobilities relative to the SnS large colloids, which display higher carrier mobility as a result of the their micrometer-scale crystalline domains. We surmise the improvement in mobility (as indicated by Figure S7) after annealing is due to a combination of these effects, and they are more significant for the SnS small and medium colloids due to their nanoscale dimensions as synthesized. The modest increase in mobility displayed by the SnS large colloids after annealing is likely accounted for by these same effects although it is less significant. Charge carriers are mostly confined to the μm-scale 2D sheets however some randomly oriented colloids might allow for interparticle charge hopping along the nanoscale thickness dimension upon removal of the ligands and surface oxide layer by annealing.

CONCLUSIONS

Three new high-yield syntheses of phase-pure colloidal SnS crystals ranging in size from the nanometer- to micrometer-scale and in shape from spherical nanoparticles to 2D sheets have been developed using solution chemistry routes. Films of each colloid type were fabricated by dropcasting and then annealed postdeposition. TRTS measurements reveal that the dropcast films composed of colloidal micrometer-sized SnS 2D sheets, as well as all three of the annealed films, undergo an initial relaxation (2−5 ps lifetimes) and charge localization/trapping processes (~60 ps lifetimes) during the first 200 ps following photoexcitation at 800 nm although further studies are needed to make unequivocal assignments. Dropcast films of the small- and medium-sized colloids do not undergo significant conductivity losses during the first 200 ps following excitation, but suffer from reduced charge carrier mobility, likely due to backscattering arising from confinement of the charge carriers to their smaller nanometer crystalline domain or grain size dimensions. Annealing improved the charge carrier mobility for all the films, with an increase of ~20% for the large sheets and up to a 5-fold improvement for the smaller nanoparticles and nanosheets. For films composed of small- and medium-sized SnS colloids, it is proposed that the improvement in mobility arises from more efficient charge transport across the domains of the film due to the removal of surface ligands, a thinner insulating surface oxide, and increased crystalline domain size. For the μm-sized SnS large film, charge transport is likely dominated by processes which occur within the 2D plane of individual colloids, but some contribution from charge transport across domain boundaries is possible for those crystals in the distribution that are randomly oriented away from the planar configuration. The slight improvement in mobility is therefore likely due to some contribution from charge hopping between neighboring crystals but could also be due to a small increase in the crystalline domain size.

The mobility values obtained here for the films of SnS colloids are comparable to values reported using contact probe techniques for SnS materials synthesized by other methods. The measured mobility of 20.3 and 23.4 cm^2/V·s in the dropcast and annealed films (at 200 ps pump delay), respectively, of the micrometer-scale SnS large sheets compares well to the 20−40 cm^2/V·s values reported for films of similar domain size.[5,28] These literature values, obtained using contact probe methods, assume long-range transport through the film which is likely afforded by large crystalline domain sizes and the absence of surface ligands. In the case of the colloidal films studied here, the charge carriers in the SnS large sheets are confined to the individual μm-scale domains over the first 200 ps, while annealing the small- and medium-sized colloids appears to allow some longer-range charge transport across the crystallite boundaries during the measured time scale. Complete decay dynamics are needed to evaluate the effect of annealing on long-range charge transport and make a better comparison to contact probe measurements.

The TRTS measurements reveal that films of SnS colloids have relatively high charge mobility depending on the colloid size dimensions but undergo loss mechanisms during the first 200 ps following visible light absorption. Initial relaxation in

DOI: 10.1021/acs.jpcc.6b01684
J. Phys. Chem. C XXXX, XXX, XXX−XXX

these films occurs in 2−5 ps, which is slightly longer than hot carrier cooling times reported in other nanoscale semiconductor materials.[42,43] This could suggest that hot charge carriers photogenerated in SnS have a better opportunity to be collected and converted to electricity before losing excess energy to heat. Collectively, high charge mobility and lengthened carrier cooling time are both advantageous for photovoltaic applications and corroborate that SnS is a viable candidate material for visible absorption and generation of free charge carriers. Further studies are required to more completely understand how to assign and control the loss mechanisms that occur on the picosecond time scale, which is essential to optimize charge transport and potentially improve the performance of future devices. For colloidal and 2D materials, control over the morphology, film thickness, and orientation of individual crystals might also be important for maximizing the efficiency of photogenerated conductivity.

■ ASSOCIATED CONTENT

Supporting Information

The Supporting Information is available free of charge on the ACS Publications website at DOI: 10.1021/acs.jpcc.6b01684.

Static electric field transmission waveforms (Figure S1), transient differential electric field transmission waveforms (Figure S2), additional TEM images of the SnS dropcast films (Figure S3), XRD patterns for the dropcast and annealed films (Figure S4), SEM images of the dropcast and annealed films (Figure S5), XPS spectra for the SnS medium dropcast and annealed films (Figure S6), fluence dependence of the calculated mobility (Figure S7), fluence dependence of the transient differential electric field transmission (Figure S8), excitation wavelength dependence of the TRTS dynamics for the SnS large dropcast film (Figure S9), fluence dependence of the decay lifetimes for the SnS large dropcast film (Figure S10), absorption spectra for the SnS colloids in suspension (Figure S11), and comparison of the TRTS dynamics between the dropcast and annealed films of the SnS large sheets (Figure S12) (PDF)

■ AUTHOR INFORMATION

Corresponding Author

*(E.J.H.) E-mail: edwin.heilweil@nist.gov. Telephone: 301-975-2370.

Notes

The authors declare no competing financial interest.

■ ACKNOWLEDGMENTS

We would like to acknowledge the NIST/National Research Council Postdoctoral Research Associateship program (B.G.A.) and NIST-STRS for funding. A.J.B. also gratefully acknowledges NIST Fellow Herbert Bennett. We thank Steven Hudson and Jeffrey Fagan for use of their instrumentation and Kerry Siebein for her helpful discussions. Certain commercial equipment or materials are identified in this paper to adequately specify the experimental procedures. In no case does the identification imply recommendation or endorsement by NIST, nor does it imply that the materials or equipment identified are necessarily the best available for the purpose.

■ REFERENCES

(1) Vigil-Galán, O.; Courel, M.; Andrade-Arvizu, J. A.; Sánchez, Y.; Espíndola-Rodríguez, M.; Saucedo, E.; Seuret-Jiménez, D.; Titsworth, M. Route towards Low Cost-High Efficiency Second Generation Solar Cells: Current Status and Perspectives. *J. Mater. Sci.: Mater. Electron.* **2015**, *26*, 5562−5573.

(2) Andrade-Arvizu, J. A.; Courel-Piedrahita, M.; Vigil-Galán, O. SnS-Based Thin Film Solar Cells: Perspectives over the Last 25 Years. *J. Mater. Sci.: Mater. Electron.* **2015**, *26*, 4541−4556.

(3) Sinsermsuksakul, P.; Sun, L.; Lee, S. W.; Park, H. H.; Kim, S. B.; Yang, C.; Gordon, R. G. Overcoming Efficiency Limitations of SnS-Based Solar Cells. *Adv. Energy Mater.* **2014**, *4*, 1400496.

(4) Albers, W.; Haas, C.; van der Maesen, F. The Preparation and the Electrical and Optical Properties of SnS Crystals. *J. Phys. Chem. Solids* **1960**, *15*, 306−310.

(5) Sinsermsuksakul, P.; Heo, J.; Noh, W.; Hock, A. S.; Gordon, R. G. Atomic Layer Deposition of Tin Monosulfide Thin Films. *Adv. Energy Mater.* **2011**, *1*, 1116−1125.

(6) Savenije, T. J.; Ferguson, A. J.; Kopidakis, N.; Rumbles, G. Revealing the Dynamics of Charge Carriers in Polymer:Fullerene Blends Using Photoinduced Time-Resolved Microwave Conductivity. *J. Phys. Chem. C* **2013**, *117*, 24085−24103.

(7) Beard, M. C.; Turner, G. M.; Schmuttenmaer, C. A. Terahertz Spectroscopy. *J. Phys. Chem. B* **2002**, *106*, 7146−7159.

(8) Baxter, J. B.; Guglietta, G. W. Terahertz Spectroscopy. *Anal. Chem.* **2011**, *83*, 4342−4368.

(9) Ulbricht, R.; Hendry, E.; Shan, J.; Heinz, T. F.; Bonn, M. Carrier Dynamics in Semiconductors Studied with Time-Resolved Terahertz Spectroscopy. *Rev. Mod. Phys.* **2011**, *83*, 543−586.

(10) Beard, M. C.; Turner, G. M.; Schmuttenmaer, C. A. Size-Dependent Photoconductivity in CdSe Nanoparticles as Measured by Time-Resolved Terahertz Spectroscopy. *Nano Lett.* **2002**, *2*, 983−987.

(11) Guglietta, G. W.; Diroll, B. T.; Gaulding, E. A.; Fordham, J. L.; Li, S.; Murray, C. B.; Baxter, J. B. Lifetime, Mobility, and Diffusion of Photoexcited Carriers in Ligand-Exchanged Lead Selenide Nanocrystal Films Measured by Time-Resolved Terahertz Spectroscopy. *ACS Nano* **2015**, *9*, 1820−1828.

(12) Turner, G. M.; Beard, M. C.; Schmuttenmaer, C. A. Carrier Localization and Cooling in Dye-Sensitized Nanocrystalline Titanium Dioxide. *J. Phys. Chem. B* **2002**, *106*, 11716−11719.

(13) Milot, R. L.; Moore, G. F.; Crabtree, R. H.; Brudvig, G. W.; Schmuttenmaer, C. A. Electron Injection Dynamics from Photoexcited Porphyrin Dyes into SnO_2 and TiO_2 Nanoparticles. *J. Phys. Chem. C* **2013**, *117*, 21662−21670.

(14) Lane, P. A.; Cunningham, P. D.; Melinger, J. S.; Kushto, G. P.; Esenturk, O.; Heilweil, E. J. Photoexcitation Dynamics in Films of C_{60} and Zn Phthalocyanine with a Layered Nanostructure. *Phys. Rev. Lett.* **2012**, *108*, 077402.

(15) Jin, Z.; Gehrig, D.; Dyer-Smith, C.; Heilweil, E. J.; Laquai, F.; Bonn, M.; Turchinovich, D. Ultrafast Terahertz Photoconductivity of Photovoltaic Polymer−Fullerene Blends: A Comparative Study Correlated with Photovoltaic Device Performance. *J. Phys. Chem. Lett.* **2014**, *5*, 3662−3668.

(16) Žídek, K.; Zheng, K.; Ponseca, C. S.; Messing, M. E.; Wallenberg, L. R.; Chábera, P.; Abdellah, M.; Sundström, V.; Pullerits, T. Electron Transfer in Quantum-Dot-Sensitized ZnO Nanowires: Ultrafast Time-Resolved Absorption and Terahertz Study. *J. Am. Chem. Soc.* **2012**, *134*, 12110−12117.

(17) Esenturk, O.; Melinger, J. S.; Heilweil, E. J. Terahertz Mobility Measurements on Poly-3-Hexylthiophene Films: Device Comparison, Molecular Weight, and Film Processing Effects. *J. Appl. Phys.* **2008**, *103*, 023102.

(18) Cunningham, P. D.; Hayden, L. M.; Yip, H.-L.; Jen, A. K.-Y. Charge Carrier Dynamics in Metalated Polymers Investigated by Optical-Pump Terahertz-Probe Spectroscopy. *J. Phys. Chem. B* **2009**, *113*, 15427−15432.

(19) Piatkowski, P.; Cohen, B.; Ponseca, C. S.; Salado, M.; Kazim, S.; Ahmad, S.; Sundström, V.; Douhal, A. Unraveling Charge Carriers Generation, Diffusion, and Recombination in Formamidinium Lead

DOI: 10.1021/acs.jpcc.6b01684
J. Phys. Chem. C XXXX, XXX, XXX−XXX

Triiodide Perovskite Polycrystalline Thin Film. *J. Phys. Chem. Lett.* **2016**, *7*, 204−210.
(20) La-o-vorakiat, C.; Salim, T.; Kadro, J.; Khuc, M.-T.; Haselsberger, R.; Cheng, L.; Xia, H.; Gurzadyan, G. G.; Su, H.; Lam, Y. M.; et al. Elucidating the Role of Disorder and Free-Carrier Recombination Kinetics in $CH_3NH_3PbI_3$ Perovskite Films. *Nat. Commun.* **2015**, *6*, 7903.
(21) Wehrenfennig, C.; Eperon, G. E.; Johnston, M. B.; Snaith, H. J.; Herz, L. M. High Charge Carrier Mobilities and Lifetimes in Organolead Trihalide Perovskites. *Adv. Mater.* **2014**, *26*, 1584−1589.
(22) Sun, L.; Miyakai, T.; Seki, S.; Dincă, M. Mn_2(2,5-Disulfhydrylbenzene-1,4-Dicarboxylate): A Microporous Metal−Organic Framework with Infinite (−Mn−S−)∞ Chains and High Intrinsic Charge Mobility. *J. Am. Chem. Soc.* **2013**, *135*, 8185−8188.
(23) Narayan, T. C.; Miyakai, T.; Seki, S.; Dincă, M. High Charge Mobility in a Tetrathiafulvalene-Based Microporous Metal−Organic Framework. *J. Am. Chem. Soc.* **2012**, *134*, 12932−12935.
(24) Alberding, B. G.; Heilweil, E. J. Time-Resolved Terahertz Spectroscopy of Electrically Conductive Metal-Organic Frameworks Doped with Redox Active Species. *Proc. SPIE* **2015**, *9567*, 95671L.
(25) Jaramillo, R.; Sher, M.-J.; Ofori-Okai, B. K.; Steinmann, V.; Yang, C.; Hartman, K.; Nelson, K. A.; Lindenberg, A. M.; Gordon, R. G.; Buonassisi, T. Transient Terahertz Photoconductivity Measurements of Minority-Carrier Lifetime in Tin Sulfide Thin Films: Advanced Metrology for an Early Stage Photovoltaic Material. *J. Appl. Phys.* **2016**, *119*, 035101.
(26) Burton, L. A.; Colombara, D.; Abellon, R. D.; Grozema, F. C.; Peter, L. M.; Savenije, T. J.; Dennler, G.; Walsh, A. Synthesis, Characterization, and Electronic Structure of Single-Crystal SnS, Sn_2S_3, and SnS_2. *Chem. Mater.* **2013**, *25*, 4908−4916.
(27) Wangperawong, A.; Herron, S. M.; Runser, R. R.; Hägglund, C.; Tanskanen, J. T.; Lee, H.-B.-R.; Clemens, B. M.; Bent, S. F. Vapor Transport Deposition and Epitaxy of Orthorhombic SnS on Glass and NaCl Substrates. *Appl. Phys. Lett.* **2013**, *103*, 052105.
(28) Chakraborty, R.; Steinmann, V.; Mangan, N. M.; Brandt, R. E.; Poindexter, J. R.; Jaramillo, R.; Mailoa, J. P.; Hartman, K.; Polizzotti, A.; Yang, C.; et al. Non-Monotonic Effect of Growth Temperature on Carrier Collection in SnS Solar Cells. *Appl. Phys. Lett.* **2015**, *106*, 203901.
(29) Walther, M.; Cooke, D. G.; Sherstan, C.; Hajar, M.; Freeman, M. R.; Hegmann, F. A. Terahertz Conductivity of Thin Gold Films at the Metal-Insulator Percolation Transition. *Phys. Rev. B: Condens. Matter Mater. Phys.* **2007**, *76*, 125408.
(30) van Exter, M.; Grischkowsky, D. Carrier Dynamics of Electrons and Holes in Moderately Doped Silicon. *Phys. Rev. B: Condens. Matter Mater. Phys.* **1990**, *41*, 12140−12149.
(31) Nienhuys, H.-K.; Sundström, V. Intrinsic Complications in the Analysis of Optical-Pump, Terahertz Probe Experiments. *Phys. Rev. B: Condens. Matter Mater. Phys.* **2005**, *71*, 235110.
(32) Ostroverkhova, O.; Cooke, D. G.; Shcherbyna, S.; Egerton, R. F.; Hegmann, F. A.; Tykwinski, R. R.; Anthony, J. E. Bandlike Transport in Pentacene and Functionalized Pentacene Thin Films Revealed by Subpicosecond Transient Photoconductivity Measurements. *Phys. Rev. B: Condens. Matter Mater. Phys.* **2005**, *71*, 035204.
(33) Ostroverkhova, O.; Shcherbyna, S.; Cooke, D. G.; Egerton, R. F.; Hegmann, F. A.; Tykwinski, R. R.; Parkin, S. R.; Anthony, J. E. Optical and Transient Photoconductive Properties of Pentacene and Functionalized Pentacene Thin Films: Dependence on Film Morphology. *J. Appl. Phys.* **2005**, *98*, 033701.
(34) Buck, M. R.; Biacchi, A. J.; Schaak, R. E. Insights into the Thermal Decomposition of Co(II) Oleate for the Shape-Controlled Synthesis of Wurtzite-Type CoO Nanocrystals. *Chem. Mater.* **2014**, *26*, 1492−1499.
(35) Biacchi, A. J.; Vaughn, D. D.; Schaak, R. E. Synthesis and Crystallographic Analysis of Shape-Controlled SnS Nanocrystal Photocatalysts: Evidence for a Pseudotetragonal Structural Modification. *J. Am. Chem. Soc.* **2013**, *135*, 11634−11644.
(36) Vaughn, D.; Sun, D.; Levin, S. M.; Biacchi, A. J.; Mayer, T. S.; Schaak, R. E. Colloidal Synthesis and Electrical Properties of GeSe Nanobelts. *Chem. Mater.* **2012**, *24*, 3643−3649.
(37) Parenteau, M.; Carlone, C. Influence of Temperature and Pressure on the Electronic Transitions in SnS and SnSe Semiconductors. *Phys. Rev. B: Condens. Matter Mater. Phys.* **1990**, *41*, 5227−5234.
(38) Park, J.; Hwang, C. H.; Lee, W. Y.; Kim, Y.; Kim, H.; Shim, I.-W. Preparation of Size-Tunable SnS Nanoparticles by a Sonochemical Method under Multibubble Sonoluminescence Conditions. *Mater. Lett.* **2014**, *117*, 188−191.
(39) Philippa, B.; Stolterfoht, M.; Burn, P. L.; Juška, G.; Meredith, P.; White, R. D.; Pivrikas, A. The Impact of Hot Charge Carrier Mobility on Photocurrent Losses in Polymer-Based Solar Cells. *Sci. Rep.* **2014**, *4*, 5695.
(40) Beard, M. C.; Turner, G. M.; Schmuttenmaer, C. A. Transient Photoconductivity in GaAs as Measured by Time-Resolved Terahertz Spectroscopy. *Phys. Rev. B: Condens. Matter Mater. Phys.* **2000**, *62*, 15764−15777.
(41) Marshall, J. M. Carrier Diffusion in Amorphous Semiconductors. *Rep. Prog. Phys.* **1983**, *46*, 1235.
(42) Lane, P. A.; Cunningham, P. D.; Melinger, J. S.; Esenturk, O.; Heilweil, E. J. Hot Photocarrier Dynamics in Organic Solar Cells. *Nat. Commun.* **2015**, *6*, 7558.
(43) Gao, Y.; Talgorn, E.; Aerts, M.; Trinh, M. T.; Schins, J. M.; Houtepen, A. J.; Siebbeles, L. D. A. Enhanced Hot-Carrier Cooling and Ultrafast Spectral Diffusion in Strongly Coupled PbSe Quantum-Dot Solids. *Nano Lett.* **2011**, *11*, 5471−5476.
(44) Schaller, R. D.; Pietryga, J. M.; Goupalov, S. V.; Petruska, M. A.; Ivanov, S. A.; Klimov, V. I. Breaking the Phonon Bottleneck in Semiconductor Nanocrystals via Multiphonon Emission Induced by Intrinsic Nonadiabatic Interactions. *Phys. Rev. Lett.* **2005**, *95*, 196401.
(45) Strait, J. H.; Wang, H.; Shivaraman, S.; Shields, V.; Spencer, M.; Rana, F. Very Slow Cooling Dynamics of Photoexcited Carriers in Graphene Observed by Optical-Pump Terahertz-Probe Spectroscopy. *Nano Lett.* **2011**, *11*, 4902−4906.
(46) Cánovas, E.; Moll, P.; Jensen, S. A.; Gao, Y.; Houtepen, A. J.; Siebbeles, L. D. A.; Kinge, S.; Bonn, M. Size-Dependent Electron Transfer from PbSe Quantum Dots to SnO2Monitored by Picosecond Terahertz Spectroscopy. *Nano Lett.* **2011**, *11*, 5234−5239.
(47) Murphy, J. E.; Beard, M. C.; Nozik, A. J. Time-Resolved Photoconductivity of PbSe Nanocrystal Arrays†. *J. Phys. Chem. B* **2006**, *110*, 25455−25461.
(48) Parkinson, P.; Lloyd-Hughes, J.; Gao, Q.; Tan, H. H.; Jagadish, C.; Johnston, M. B.; Herz, L. M. Transient Terahertz Conductivity of GaAs Nanowires. *Nano Lett.* **2007**, *7*, 2162−2165.
(49) Bergren, M. R.; Kendrick, C. E.; Neale, N. R.; Redwing, J. M.; Collins, R. T.; Furtak, T. E.; Beard, M. C. Ultrafast Electrical Measurements of Isolated Silicon Nanowires and Nanocrystals. *J. Phys. Chem. Lett.* **2014**, *5*, 2050−2057.
(50) http://rsbweb.nih.gov/ij/.

DOI: 10.1021/acs.jpcc.6b01684
J. Phys. Chem. C XXXX, XXX, XXX−XXX